Journal of
Materials Chemistry C

PAPER

Published on 13 April 2016
Licence and permissions

Cite this: J. Mater. Chem. C, 2016, 4, 4538

Strain-induced enhancement in the thermoelectric performance of a ZrS_2 monolayer

H. Y. Lv,[a] W. J. Lu,*[a] D. F. Shao,[a] H. Y. Lu[b] and Y. P. Sun*[acd]

Received 18th March 2016,
Accepted 13th April 2016

DOI: 10.1039/c6tc01135g

www.rsc.org/MaterialsC

The increase of a thermoelectric material's figure of merit (*ZT* value) is limited by the interplay of the transport coefficients. Here we report the greatly enhanced thermoelectric performance of a ZrS_2 monolayer by the biaxial tensile strain, due to the simultaneous increase of the Seebeck coefficient and decrease of the thermal conductivity. Based on first-principles calculations combined with the Boltzmann transport theory, we predict that the band structure of the ZrS_2 monolayer can be effectively engineered by the strain, and the Seebeck coefficient is significantly increased. The thermal conductivity is reduced by the applied tensile strain due to the phonon softening. At the strain of 6%, the maximum *ZT* value of 2.4 is obtained for the p-type doped ZrS_2 monolayer at 300 K, which is 4.3 times larger than that of the unstrained system. Moreover, the temperature dependence of the *ZT* values is investigated, and compared with the unstrained system, the *ZT* values of the p- and n-type doping are much more balanced by the applied strain.

1 Introduction

Thermoelectric devices can directly convert heat energy to electricity and *vice versa*, and thus have promising applications in solid-state cooling and power generation. The efficiency of a thermoelectric device is determined by the thermoelectric material's dimensionless figure of merit

$$ZT = S^2\sigma T/(\kappa_e + \kappa_p), \quad (1)$$

where S, σ, T, κ_e and κ_p are the Seebeck coefficient, electrical conductivity, absolute temperature, electronic and lattice thermal conductivities, respectively. Because the transport coefficients (S, σ, κ_e and κ_p) are strongly coupled to each other, none of them can be independently tuned to largely enhance the thermoelectric performance.

It was theoretically proposed that one- (1D) or two-dimensional (2D) materials could have much larger *ZT* values than their bulk counterparts.[1,2] In recent years, with the rapid pace of progress in nanotechnologies, a large variety of low-dimensional materials beyond graphene have been successfully prepared.[3,4] Among them, single layers of transition metal dichalcogenides (TMDCs) have received a lot of attention because some of them, such as MoS_2, are semiconductors with sizable direct band gaps, making them promising candidates for application in field effect transistors[5] and optoelectronic devices.[6] In addition, MX_2 (M = Mo, W; X = S, Se) monolayers were reported to have much improved thermoelectric performance compared to the corresponding bulks,[7–10] opening up a new opportunity of TMDCs monolayers in the thermoelectric field.

The ZrS_2 monolayer is another typical 2D TMDC and has been successfully synthesized experimentally.[11] It was predicted that the thermal conductivity of the ZrS_2 monolayer is much lower than those of MX_2 (M = Mo, W; X = S, Se) monolayers,[12] which is desirable for the thermoelectric application. However, the thermoelectric performance of the ZrS_2 monolayer has not been explored. Recently, it was reported that the electronic structure of the ZrS_2 monolayer could be tuned by external strains.[13] In previous reports, strain has proven to be a flexible and effective method to tune the electronic,[14–17] phonon,[18,19] and thus the thermoelectric properties of 2D systems. For example, the Seebeck coefficient of phosphorene can be greatly enhanced due to strain-induced band convergence.[17] The thermal conductivity can be either increased[18] or reduced[19] by the applied strains, depending on the particular material. It is thus interesting to investigate the thermoelectric performance of the ZrS_2 monolayer and how it will be influenced by the external strain. In this work, by using the first-principles calculations combined with the Boltzmann transport theory, we predict that the ZrS_2 monolayer could be a very promising candidate for the thermoelectric application. In addition, the

[a] Key Laboratory of Materials Physics, Institute of Solid State Physics, Chinese Academy of Sciences, Hefei 230031, People's Republic of China. E-mail: wjlu@issp.ac.cn, ypsun@issp.ac.cn; Fax: +86-551-65591434; Tel: +86-551-65591439
[b] School of Physics and Electronic Information, Huaibei Normal University, Huaibei 235000, People's Republic of China
[c] High Magnetic Field Laboratory, Chinese Academy of Sciences, Hefei 230031, People's Republic of China
[d] Collaborative Innovation Center of Advanced Microstructures, Nanjing University, Nanjing, 210093, People's Republic of China

This journal is © The Royal Society of Chemistry 2016

thermoelectric performance of the ZrS_2 monolayer can be significantly improved by the biaxial tensile strain, due to the simultaneous increase of the Seebeck coefficient and decrease of the thermal conductivity.

2 Computational details

The structural and electronic properties of the ZrS_2 monolayer were calculated within the framework of the density functional theory (DFT),[20] as implemented in the ABINIT code.[21–23] The projector augmented-wave (PAW) pseudopotential approach was used. The exchange–correlation potential was in the form of the Perdew–Burke–Ernzerhof (PBE) expression[24] of the generalized-gradient approximation (GGA). The spin–orbital coupling was included in the calculations of electronic properties. The cutoff energy was set to be 600 eV. For each monolayer, a vacuum region of 15 Å was added so that the interactions between the monolayer and its period image can be neglected. The Brillouin zones were sampled using $7 \times 7 \times 1$ and $10 \times 10 \times 1$ Monkhorst–Pack k meshes for the structural relaxation and electronic structure calculations, respectively.

The electronic transport coefficients are derived from the electronic structure based on the semiclassical Boltzmann transport theory in the relaxation time approximation, as implemented in the BOLTZTRAP code.[25] The Seebeck coefficient S and electrical conductivity σ are given by

$$S(\mu, T) = \frac{ek_B}{\sigma}\int d\varepsilon\left(-\frac{\partial f_\mu(T,\varepsilon)}{\partial\varepsilon}\right)\Xi(\varepsilon)\frac{\varepsilon-\mu}{k_B T}, \quad (2)$$

$$\sigma(\mu, T) = e^2\int d\varepsilon\left(-\frac{\partial f_\mu(T,\varepsilon)}{\partial\varepsilon}\right)\Xi(\varepsilon), \quad (3)$$

where f_μ is the Fermi–Dirac distribution function $f_\mu(T,\varepsilon) = \frac{1}{e^{(\varepsilon-\mu)/k_B T}+1}$, k_B is Boltzmann's constant, and μ is the chemical potential. The kernel is to calculate the transport distribution $\Xi(\varepsilon)$, which is expressed as

$$\Xi(\varepsilon) = \sum_{\mathbf{k}} \mathbf{v}_{\mathbf{k}} \otimes \mathbf{v}_{\mathbf{k}}\tau_{\mathbf{k}}, \quad (4)$$

where $\mathbf{v}_{\mathbf{k}}$ and $\tau_{\mathbf{k}}$ are the group velocity and relaxation time at state $\mathbf{k}$, respectively. Doping is treated within the rigid band picture.[26] The electronic thermal conductivity is calculated by the Wiedemann–Franz law $\kappa_e = L\sigma T$, where L is the Lorenz number. Here we use a Lorenz number of 1.5×10^{-8} WΩ K^{-2}.[27]

In the phonon calculations, the force constant matrices were calculated *via* density functional perturbation theory (DFPT) as implemented in the VASP code.[28–30] A $5 \times 5 \times 1$ superlattice was used. Phonon frequencies were obtained using the PHONOPY program.[31] The lattice thermal conductivity was calculated by solving the phonon Boltzmann transport equation within the relaxation time approximation, as implemented in the ShengBTE code.[32] The second order harmonic and third order anharmonic interatomic force constants (IFCs) were calculated by using a $5 \times 5 \times 1$ supercell with $2 \times 2 \times 1$ Monkhorst–Pack k meshes and a $4 \times 4 \times 1$ supercell with Γ point, respectively. The interactions up to third-nearest neighbors were considered when calculating the third order IFCs.

3 Results and discussion

3.1 Energy-band structure

Bulk ZrS_2 crystallizes in a layered structure with the space group $P\bar{3}m1$, as shown in Fig. 1(a). Because of the weak van der Waals interactions between the S–Zr–S sandwich layers, it is possible to exfoliate a few layers or even a monolayer of ZrS_2 from the bulk structure.[11] The top and side views of the ZrS_2 monolayer are shown in Fig. 1(b) and (c), respectively. After full relaxation, the lattice parameters are $a = b = 3.676$ Å, slightly larger than the experimental values of the ZrS_2 bulk.[33]

The ZrS_2 monolayer is a semiconductor, with the valence band maximum (VBM) and conduction band minimum (CBM) located at Γ and M points, respectively, as shown in Fig. 2(c). The indirect band gap is calculated to be 1.10 eV, in good agreement with the previous report.[13] Next, we will investigate the strain effect on the electronic structure of the ZrS_2 monolayer. Here the in-plane biaxial strain is considered, which is defined as $\varepsilon = (a - a_0)/a_0 \times 100\%$, where a and a_0 are the in-plane lattice constants of the strained and unstrained monolayers, respectively. When the tensile strain is applied, as shown in Fig. 2, the VBM is gradually lowered while the CBM is elevated as the increasing strain, resulting in the increased band gap of the strained ZrS_2 monolayer (see Fig. 3). When the strain reaches 6%, the VBM moves from the Γ point to the one along the K–Γ direction and the band gap reaches a maximum value of 1.63 eV. When further increasing the strain, the CBM moves from the M point to the Γ point. Moreover, the VBM is gradually elevated and the CBM is lowered, leading to the decreased band gap when the strain is larger than 6%. The ZrS_2 monolayer remains an indirect-band-gap semiconductor up to the strain of 10%. On the other hand, when the strain is compressive, the band gap decreases monotonically as increasing the strain. At the strain of −8%, the ZrS_2 monolayer tends to be a metal and the semiconductor-to-metal transition takes place. The strain tunable electronic structure of the ZrS_2

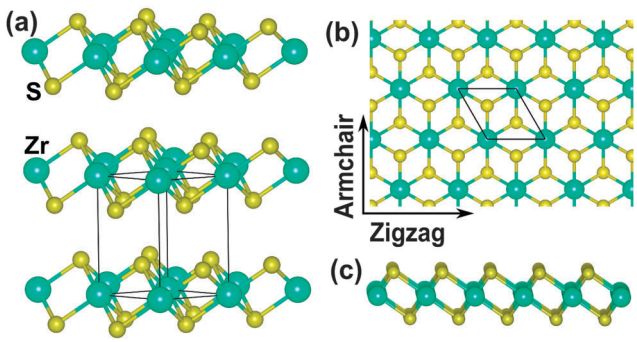

Fig. 1 (a) Crystal structure of the ZrS_2 bulk; (b) top and (c) side views of the ZrS_2 monolayer. The black lines in (a) and (b) denote the primitive cells of the bulk and monolayer ZrS_2, respectively.

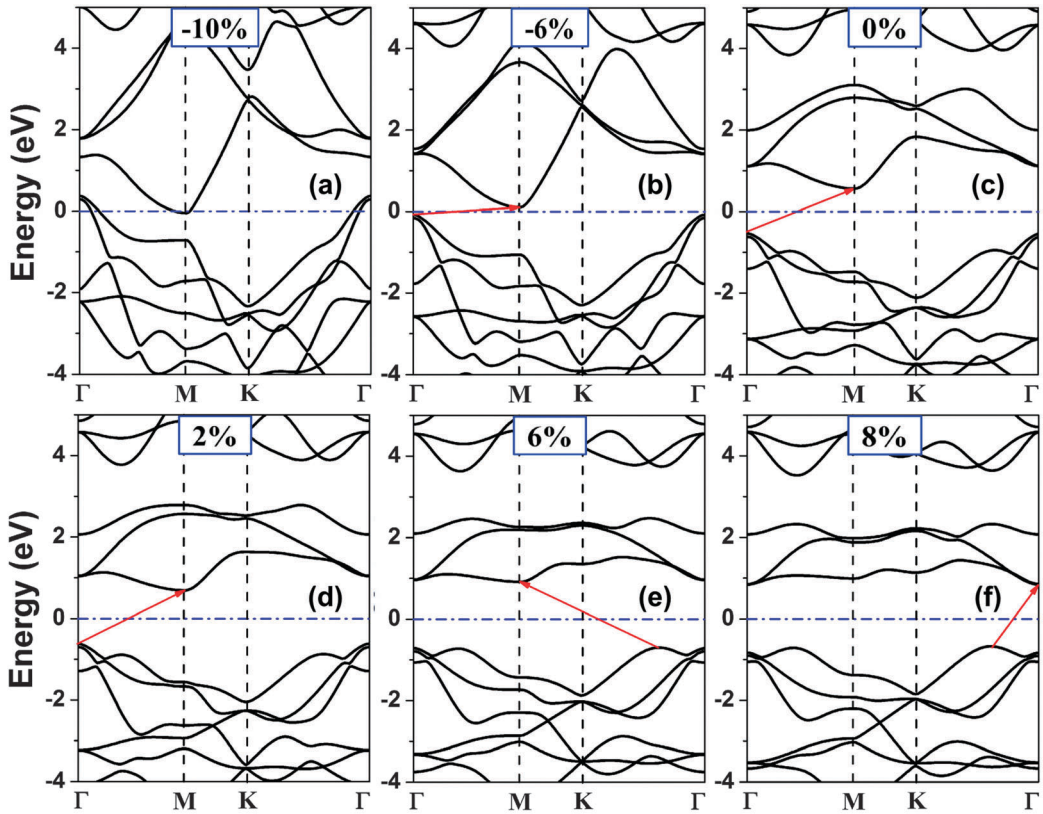

Fig. 2 Band structures of the ZrS_2 monolayer under different biaxial strains. The red arrows point from the valence band maximum to the conduction band minimum. The Fermi level is set to be 0 eV.

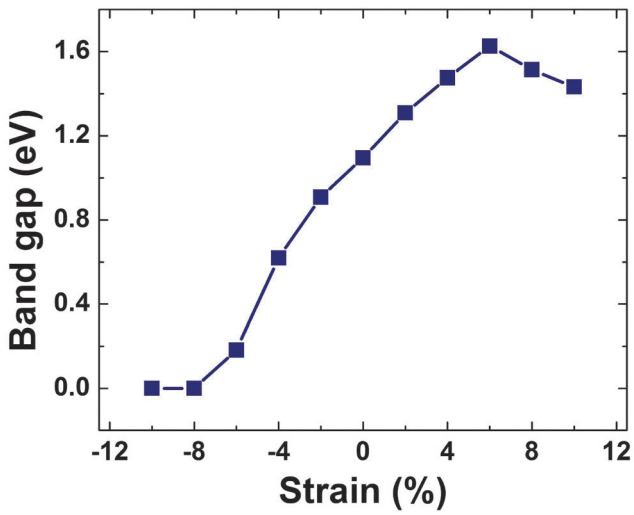

Fig. 3 Calculated band gap of the ZrS_2 monolayer as a function of the applied biaxial strain.

monolayer will significantly influence the electronic transport properties, which will be discussed in the following.

3.2 Electronic transport coefficients

Based on the calculated electronic structure, we are able to evaluate the electronic transport coefficients by using the semiclassical Boltzmann transport theory and the rigid-band model. Within this method, the Seebeck coefficient S can be calculated independent of the relaxation time τ; however, the electrical conductivity σ is calculated with τ inserted as a parameter, that is, what we obtain is σ/τ. In Fig. 4, we plot the calculated electronic transport coefficients of the ZrS_2 monolayer as a function of the carrier concentration under different strains. The results for the zigzag and armchair directions are the same (due to the high structural symmetry of the ZrS_2 monolayer), so the transporting directions are not distinguished here. From Fig. 4(a), we can see that the compressive strains have little impact on the Seebeck coefficient of the p-type doped system while they reduce the Seebeck coefficient of the n-type doped one. For the tensile strain, the maximum absolute values of the Seebeck coefficients of both the p- and n-type doped systems first increase as the increasing strain, reach the maximum at the strain of 6% and then decrease when the strain is further increased. If we notice the strain-dependence of the band gap (see Fig. 3), we can see that such a trend of the Seebeck coefficient coincides with that of the band gap. Therefore, the Seebeck coefficient is efficiently tuned by the strain *via* the band structure engineering. The greatly increased Seebeck coefficient of the ZrS_2 monolayer is very favorable for thermoelectric application.

Fig. 4(b) shows the electrical conductivity σ/τ as a function of the carrier concentration. When the doping is not very high

 This journal is © The Royal Society of Chemistry 2016

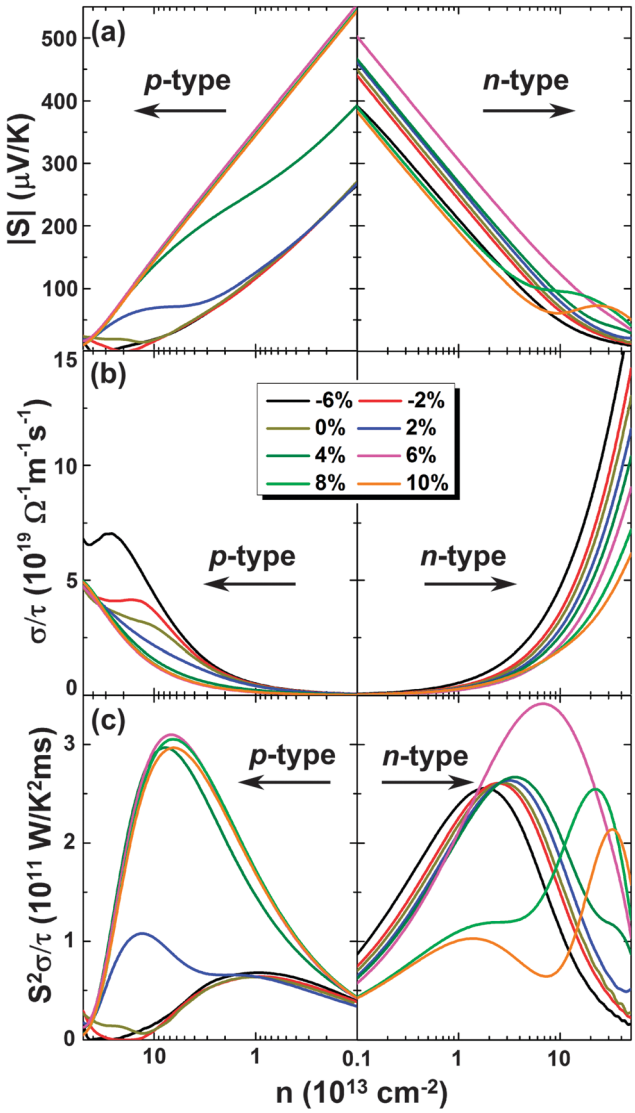

Fig. 4 (a) Absolute values of the Seebeck coefficient, (b) electrical conductivity and (c) power factor of the ZrS_2 monolayer as a function of the carrier concentration under different biaxial strains.

($n < 10^{14}$ cm^{-2}), σ/τ generally decreases as the increasing band gap, which is in contrast to the tendency of the Seebeck coefficient. The decrease of the electrical conductivity is detrimental to the thermoelectric performance. Whether the applied strain will benefit the electronic transport properties or not will be determined by the competition of the two factors. In Fig. 4(c), we plot the power factors of the ZrS_2 monolayer under different strains. For the tensile strain, the maximum power factor generally increases as the increasing band gap, indicating that the increase of the Seebeck coefficient outweighs the negative effect from the electrical conductivity. For the p-type doped ZrS_2 monolayer, the power factor is significantly increased by the applied tensile strain. Compared with the unstrained system, in which the power factor of the n-type doping is much larger than that of the p-type one, the tensile strain makes the power factors of the p- and n-type doped systems more balanced.

As mentioned above, within our method, the electrical conductivity σ can only be calculated with the relaxation time τ inserted. The relaxation time is determined by

$$\mu = e\tau/m^*, \tag{5}$$

where μ is the carrier mobility and m^* is the effective mass. The carrier mobility μ of the ZrS_2 monolayer can be calculated using the deformation potential (DP) theory based on the effective mass approximation:[34–36]

$$\mu = \frac{e\hbar^3 C}{k_B T m^* m_d E_1^2}, \tag{6}$$

where m_d is the average effective mass defined by $m_d = \sqrt{m_x^* m_y^*}$. C is the elastic modulus and can be determined by $C = (\partial^2 E/\partial\delta^2)/S_0$, where E, δ, and S_0 are, respectively, the total energy, the applied strain, and the area of the investigated system. The DP constant E_1 is obtained by $E_1 = dE_{edge}/d\delta$, where δ is the applied strain by a step of 0.5% and E_{edge} is the energy of the band edges (VBM for the holes and CBM for the electrons). Since the ZrS_2 monolayer has the largest power factor at the strain of 6%, we will only consider this strain condition. The calculated m^*, m_d, C, E_1, and the room-temperature μ and relaxation time τ of the unstrained and 6% strained ZrS_2 monolayers are summarized in Table 1. For the unstrained case, the effective mass of the electron along the armchair direction is much larger than that along the zigzag direction, since the conduction band dispersion around the M point is highly anisotropic (see Fig. 2(c)), that is, the conduction band is much flatter along the Γ–M direction (armchair direction in real space) than that along the M–K direction (zigzag direction in the real space). However, the

Table 1 Effective mass (m^*), average effective mass (m_d), elastic modulus C, DP constant E_1, carrier mobility (μ), relaxation time (τ) at 300 K in the zigzag and armchair directions of the unstrained and 6% strained ZrS_2 monolayers

			m^* (m_e)	m_d (m_e)	C (eV (Å^{-2}))	E_1 (eV)	μ (cm^2 V^{-1} s^{-1})	τ (10^{-13} s)
Unstrained	Zigzag	e	0.28	0.74	6.36	−3.17	1045.3	1.66
		h	−0.27	0.26	6.36	−6.67	695.8	1.07
	Armchair	e	1.97	0.74	6.34	−3.99	93.3	1.04
		h	−0.26	0.26	6.34	−6.46	769.2	1.14
Strained	Zigzag	e	0.43	1.13	6.36	−4.02	276.7	0.68
		h	−0.72	0.80	6.36	−3.61	289.3	1.18
	Armchair	e	2.97	1.13	6.34	−3.73	46.5	0.79
		h	−0.90	0.80	6.34	−3.66	225.3	1.15

valence band dispersion around the Γ point is nearly isotropic, which results in the almost same effective masses of the hole along the zigzag and armchair directions. The case for the strained ZrS_2 monolayer is similar, except that the corresponding effective masses are enhanced by the strain. The elastic modulus C and DP constant E_1 for both the electron and hole have little difference along the two directions. Accordingly, the anisotropy of the carrier mobilities is dominated by the corresponding anisotropy of the carrier effective masses. For the electron, the mobility along the zigzag direction is much larger than that along the armchair direction. The electron mobility along the zigzag direction of the unstrained system is 1045.3 $cm^2 V^{-1} s^{-1}$, comparing favorably with that of the MoS_2 monolayer.[37] The applied strain reduces both the electron and hole mobilities, mainly due to the increased effective masses. Based on eqn (5) and (6), the relaxation time τ will depend on the average effective mass m_d but not m^*, so the anisotropy of m^* will not be reflected in τ. As a result, there is little difference in the relaxation time τ along different directions. In the following, we will use the averaged τ of the two directions to estimate the thermoelectric performance.

3.3 Lattice thermal conductivity

Next, we will investigate the strain effect on the thermal transport properties of the ZrS_2 monolayer. The lattice thermal conductivities κ_p of the unstrained and 6% strained ZrS_2 monolayers are shown in Fig. 5(a). For both cases, the κ_p decreases as the increasing temperature, following a T^{-1} dependence, as indicated by the fitting lines in the figure. This implies that the dominant scattering mechanism is the Umklapp process. Moreover, in the temperature range investigated, the thermal conductivities of the 6% strained ZrS_2 monolayer are much smaller than those of the unstrained system. In particular, at 300 K, the κ_p decreases from 3.29 to 1.99 W m^{-1} K^{-1}, reduced by 40% when the strain of 6% is applied. To investigate the origin of the reduction in the thermal conductivity, in Fig. 5(b), we plot the corresponding phonon dispersions. At the strain of 6%, the phonon dispersions of transverse and longitudinal acoustic (TA and LA) modes become softened, while the out-of-plane acoustic (ZA) mode is slightly stiffened. The contribution of each phonon mode to the total thermal conductivity can be expressed as

$$\kappa_i(\mathbf{q}) = C_i(\mathbf{q})\nu_i^2(\mathbf{q})\tau_i(\mathbf{q}), \tag{7}$$

where C_i, ν_i, and τ_i are the specific heat, group velocity and phonon relaxation time, respectively; $\mathbf{q}$ is the wave vector. Our results show that the three acoustic phonon branches contribute mostly to the thermal conductivity, so we will only focus on the acoustic modes in the following. The insets of Fig. 5(c) and (d) are the calculated group velocities of the different modes for the unstrained and 6% strained ZrS_2 monolayers, respectively. We can see that when the 6% strain is applied, the

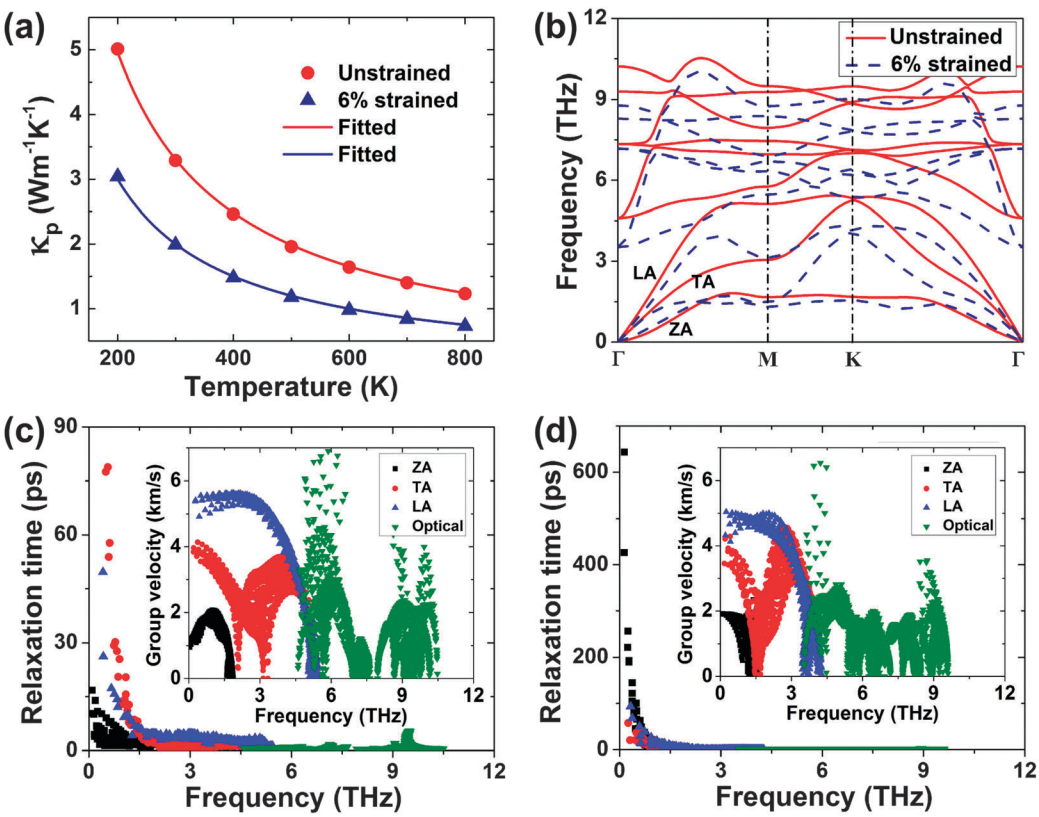

Fig. 5 (a) Temperature dependence of the lattice thermal conductivities and (b) phonon dispersions of the unstrained and 6% strained ZrS_2 monolayers; phonon relaxation times for (c) unstrained and (d) 6% strained systems. The insets in (c) and (d) are the corresponding group velocities.

 This journal is © The Royal Society of Chemistry 2016

group velocity of the ZA mode is slightly increased while those of the TA and LA modes are decreased compared with the unstrained case. This is reasonable since the group velocity is calculated based on $\nu_i(\mathbf{q}) = \frac{\partial\omega}{\partial\mathbf{q}}$. Therefore, the phonon softening leads to the reduced group velocity, which will be a source of the reduction in the lattice thermal conductivity. In contrast, the phonon stiffening will increase the κ_p. On the other hand, we can see from Fig. 5(c) and (d) that compared with the unstrained ZrS_2 monolayer, the relaxation times of the strained system are generally increased, which will however benefit the lattice thermal conductivity. The above competing factors indicating that the decreased group velocities of the TA and LA modes originating from the phonon softening predominate in determining the reduced lattice thermal conductivity of the strained ZrS_2 monolayer.

3.4 Figure of merit

Combining the electronic and thermal transport properties, we now evaluate the thermoelectric performance of the ZrS_2 monolayer. The room-temperature *ZT* values of the unstrained and 6% strained systems are shown in Fig. 6. For the unstrained ZrS_2 monolayer, the maximum *ZT* value of the n-type doped system is much larger than that of the p-type doped one. When the strain of 6% is applied, the maximum *ZT* value of 2.4 is obtained for the p-type doping, which is 4.3 times larger than that of the unstrained system. For the n-type doping, the enhancement of the maximum *ZT* value is relatively smaller, from 1.7 for the unstrained system to 1.8 for the 6% strained one. The increase of the Seebeck coefficient as well as the decrease of the lattice thermal conductivity contributes simultaneously to the enhanced thermoelectric performance.

3.5 Temperature dependence

To investigate the temperature dependence of the thermoelectric performance, we plot in Fig. 7 the absolute values of the Seebeck coefficients at the optimal doping level and the maximum *ZT* values as a function of the temperature ranging from 200 to 800 K. For both the unstrained and 6% strained ZrS_2 monolayers, the Seebeck coefficients and *ZT* values increase monotonically with the increase in temperature. We have also investigated the electrical conductivities at the optimal doping level, which however decrease as the increasing temperature. Therefore, when the temperature is elevated, the increase of the maximum *ZT* value originates from the increase of the Seebeck coefficient and decrease of the lattice thermal conductivity. Moreover, for the unstrained case, the *ZT* value of the n-type doping is much larger than that of the p-type doping in the temperature range investigated. The difference of the *ZT* values between the n- and p-type doping becomes larger and larger with the increase of the temperature. At 800 K, the *ZT* values of 2.3 and 4.8 are obtained for the p- and n-type doping, respectively. For the 6% strained system, however, the *ZT* value of the p-type doping is relatively larger than that of the n-type doping and the difference becomes smaller and smaller as the increasing temperature. At 800 K, the *ZT* values reach the maximum of 5.1, identical for the p- and n-type doping. The much more balanced *ZT* values of the 6% strained system are very desirable for the fabrication of thermoelectric modulus with both p- and n-legs.

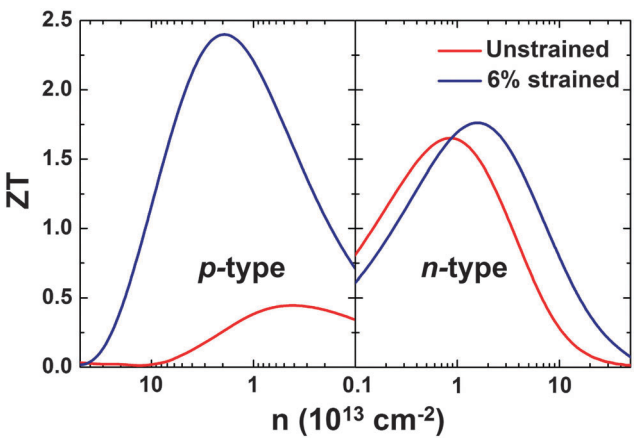

Fig. 6 *ZT* values at 300 K as a function of the carrier concentration of the unstrained and 6% strained ZrS_2 monolayers.

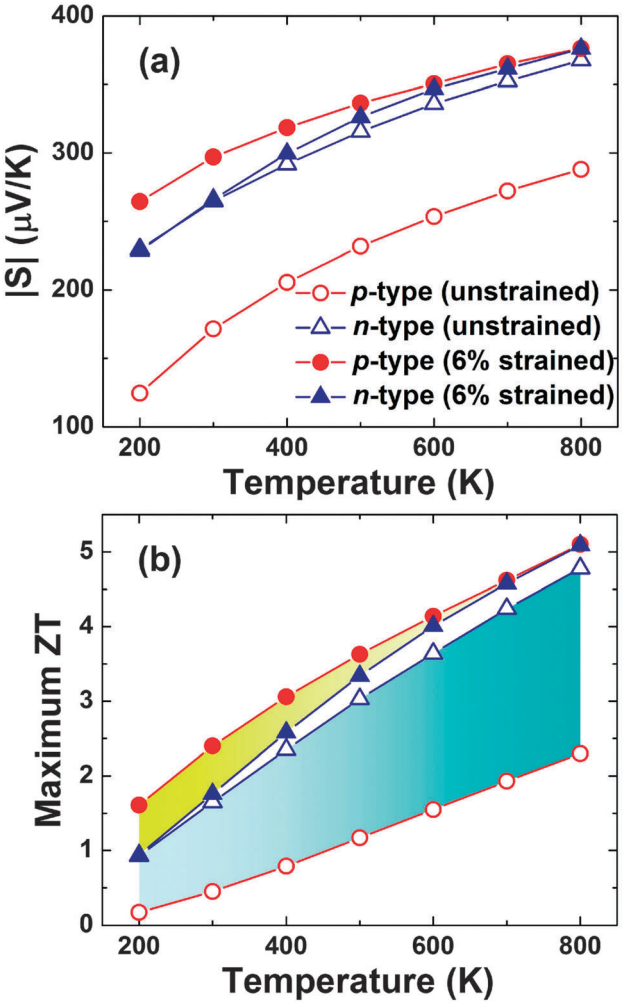

Fig. 7 Temperature dependence of (a) absolute values of the Seebeck coefficients at the optimal doping level and (b) maximum *ZT* values of the p- and n-type doping for the unstrained and 6% strained ZrS_2 monolayers.

4 Conclusion

In summary, we have investigated the strain effect on the electronic, phonon, and thermoelectric properties of the ZrS_2 monolayer. The band gap first increases and then decreases as the increasing biaxial strain, reaching the maximum at the strain of 6%. The Seebeck coefficient of the ZrS_2 monolayer is found to be effectively tuned by the strain *via* the band structure engineering. The increase of the Seebeck coefficient outweighs the decrease of the electrical conductivity and thus the maximum power factor of the ZrS_2 monolayer increases as the increasing band gap. At the strain of 6%, the thermoelectric performance of the ZrS_2 monolayer is greatly enhanced, due to the simultaneous increase of the Seebeck coefficient and decrease of the thermal conductivity. Moreover, the *ZT* value increases monotonically with the increase of temperature. Compared with the unstrained system, the *ZT* values of the p- and n-type doping are much more balanced by the applied strain. Our results show that the applied strain is an efficient method for improving the thermoelectric performance of the ZrS_2 monolayer.

In experiments, strain can be applied to a 2D material in different ways. For example, strain can be induced by the lattice mismatch between the epitaxial thin films and substrates.[38] Moreover, one can also transfer a 2D material to a soft supporting substrate and apply strain to the 2D system by bending[39] or stretching[40] the substrate. On the other hand, the doping of the 2D material could be achieved by adsorption of small molecules, and electrons can be donated to (n-type doping) or withdrawn from (p-type doping) the 2D material, depending on the different electron affinities between the dopants and the 2D system.[41,42] In addition, the site atoms can be substituted by other atoms. When the substitutional atom has less (more) valence electrons than that of the site atom, the doping is p-type (n-type).[43] The system can also be doped by electrolyte gating,[44,45] which is a clean method without the introduction of randomly distributed impurities. These methods can be readily transferred to the ZrS_2 monolayer. The system investigated is a very promising candidate for thermoelectric application, which deserves further study by experiment.

Acknowledgements

This work was supported by the National Natural Science Foundation of China under Contracts No. 11274311, 11404340, and U1232139, the Anhui Provincial Natural Science Foundation under Contract No. 1408085MA11, the China Postdoctoral Science Foundations (Grant No. 2014M550352 and 2015T80670), and the Youth Innovation Promotion Association of CAS (2012310). The calculation was partially performed at the Center for Computational Science, CASHIPS.

References

1 L. D. Hicks and M. S. Dresselhaus, *Phys. Rev. B: Condens. Matter Mater. Phys.*, 1993, **47**, 12727–12731.
2 L. D. Hicks and M. S. Dresselhaus, *Phys. Rev. B: Condens. Matter Mater. Phys.*, 1993, **47**, 16631–16634.
3 J. N. Coleman, M. Lotya, A. O'Neill, S. D. Bergin, P. J. King, U. Khan, K. Young, A. Gaucher, S. De, R. J. Smith, I. V. Shvets, S. K. Arora, G. Stanton, H.-Y. Kim, K. Lee, G. T. Kim, G. S. Duesberg, T. Hallam, J. J. Boland, J. J. Wang, J. F. Donegan, J. C. Grunlan, G. Moriarty, A. Shmeliov, R. J. Nicholls, J. M. Perkins, E. M. Grieveson, K. Theuwissen, D. W. McComb, P. D. Nellist and V. Nicolosi, *Science*, 2011, **331**, 568–571.
4 S. Jeong, D. Yoo, M. Ahn, P. Miró, T. Heine and J. Cheon, *Nat. Commun.*, 2015, **6**, 5763.
5 B. Radisavljevic, A. Radenovic, J. Brivio, V. Giacometti and A. Kis, *Nat. Nanotechnol.*, 2011, **6**, 147–150.
6 O. Lopez-Sanchez, D. Lembke, M. Kayci, A. Radenovic and A. Kis, *Nat. Nanotechnol.*, 2013, **8**, 497–501.
7 M. Buscema, M. Barkelid, V. Zwiller, H. S. J. van der Zant, G. A. Steele and A. Castellanos-Gomez, *Nano Lett.*, 2013, **13**, 358–363.
8 W. Huang, H. Da and G. Liang, *J. Appl. Phys.*, 2013, **113**, 104304.
9 D. Wickramaratne, F. Zahid and R. K. Lake, *J. Chem. Phys.*, 2014, **140**, 124710.
10 H. Babaei, J. M. Khodadadi and S. Sinha, *Appl. Phys. Lett.*, 2014, **105**, 193901.
11 Z. Zeng, Z. Yin, X. Huang, H. Li, Q. He, G. Lu, F. Boey and H. Zhang, *Angew. Chem., Int. Ed.*, 2011, **50**, 11093–11097.
12 X. Gu and R. Yang, *Appl. Phys. Lett.*, 2014, **105**, 131903.
13 Y. Li, J. Kang and J. Li, *RSC Adv.*, 2014, **4**, 7396–7401.
14 Z. H. Ni, T. Yu, Y. H. Lu, Y. Y. Wang, Y. P. Feng and Z. X. Shen, *ACS Nano*, 2008, **2**, 2301–2305.
15 K. He, C. Poole, K. F. Mak and J. Shan, *Nano Lett.*, 2013, **13**, 2931–2936.
16 R. Fei and L. Yang, *Nano Lett.*, 2014, **14**, 2884–2889.
17 H. Y. Lv, W. J. Lu, D. F. Shao and Y. P. Sun, *Phys. Rev. B: Condens. Matter Mater. Phys.*, 2014, **90**, 085433.
18 M. Hu, X. Zhang and D. Poulikakos, *Phys. Rev. B: Condens. Matter Mater. Phys.*, 2013, **87**, 195417.
19 L. Zhu, T. Zhang, Z. Sun, J. Li, G. Chen and S. A. Yang, *Nanotechnology*, 2015, **26**, 465707.
20 P. Hohenberg and W. Kohn, *Phys. Rev.*, 1964, **136**, B864–B871.
21 X. Gonze, J.-M. Beuken, R. Caracas, F. Detraux, M. Fuchs, G.-M. Rignanese, L. Sindic, M. Verstraete, G. Zerah, F. Jollet, M. Torrent, A. Roy, M. Mikami, P. Ghosez, J.-Y. Raty and D. C. Allan, *Comput. Mater. Sci.*, 2002, **25**, 478–492.
22 X. Gonze, G.-M. Rignanese, M. Verstraete, J.-M. Beuken, Y. Pouillon, R. Caracas, F. Jollet, M. Torrent, G. Zerah, M. Mikami, P. Ghosez, M. Veithen, J.-Y. Raty, V. Olevano, F. Bruneval, L. Reining, R. Godby, G. Onida, D. R. Hamann and D. C. Allan, *Z. Kristallogr.*, 2005, **220**, 558–562.
23 X. Gonze, *et al.*, *Comput. Phys. Commun.*, 2009, **180**, 2582–2615.
24 J. P. Perdew, K. Burke and M. Ernzerhof, *Phys. Rev. Lett.*, 1996, **77**, 3865–3868.
25 G. K. H. Madsen and D. J. Singh, *Comput. Phys. Commun.*, 2006, **175**, 67–71.
26 E. A. Stern, *Phys. Rev.*, 1967, **157**, 544–551.

 This journal is © The Royal Society of Chemistry 2016

27 R. Venkatasubramanian, E. Siivola, T. Colpitts and B. O'Quinn, *Nature*, 2001, **413**, 597–602.
28 G. Kresse and J. Hafner, *Phys. Rev. B: Condens. Matter Mater. Phys.*, 1993, **47**, 558–561.
29 G. Kresse and J. Hafner, *Phys. Rev. B: Condens. Matter Mater. Phys.*, 1994, **49**, 14251–14269.
30 G. Kresse and J. Furthmüller, *Comput. Mater. Sci.*, 1996, **6**, 15–50.
31 A. Togo and I. Tanaka, *Scr. Mater.*, 2015, **108**, 1–5.
32 W. Li, J. Carrete, N. A. Katcho and N. Mingo, *Comput. Phys. Commun.*, 2014, **185**, 1747–1758.
33 D. L. Greenaway and R. Nitsche, *J. Phys. Chem. Solids*, 1965, **26**, 1445–1458.
34 S.-i. Takagi, A. Toriumi, M. Iwase and H. Tango, *IEEE Trans. Electron Devices*, 1994, **41**, 2357–2362.
35 S. Bruzzone and G. Fiori, *Appl. Phys. Lett.*, 2011, **99**, 222108.
36 J. Qiao, X. Kong, Z.-X. Hu, F. Yang and W. Ji, *Nat. Commun.*, 2014, **5**, 4475.
37 B. Radisavljevic and A. Kis, *Nat. Mater.*, 2013, **12**, 815–820.
38 G. Gao, S. Jin and W. Wu, *Appl. Phys. Lett.*, 2007, **90**, 012509.
39 S.-I. Park, J.-H. Ahn, X. Feng, S. Wang, Y. Huang and J. A. Rogers, *Adv. Funct. Mater.*, 2008, **18**, 2673–2684.
40 K. S. Kim, Y. Zhao, H. Jang, S. Y. Lee, J. M. Kim, K. S. Kim, J.-H. Ahn, P. Kim, J.-Y. Choi and B. H. Hong, *Nature*, 2009, **457**, 706–710.
41 S. Mouri, Y. Miyauchi and K. Matsuda, *Nano Lett.*, 2013, **13**, 5944–5948.
42 D. Kiriya, M. Tosun, P. Zhao, J. S. Kang and A. Javey, *J. Am. Chem. Soc.*, 2014, **136**, 7853–7856.
43 M. R. Laskar, D. N. Nath, L. Ma, E. W. Lee II, C. H. Lee, T. Kent, Z. Yang, R. Mishra, M. A. Roldan, J.-C. Idrobo, S. T. Pantelides, S. J. Pennycook, R. C. Myers, Y. Wu and S. Rajan, *Appl. Phys. Lett.*, 2014, **104**, 092104.
44 A. Das, S. Pisana, B. Chakraborty, S. Piscanec, S. K. Saha, U. V. Waghmare, K. S. Novoselov, H. R. Krishnamurthy, A. K. Geim, A. C. Ferrari and A. K. Sood, *Nat. Nanotechnol.*, 2008, **3**, 210–215.
45 J. T. Ye, Y. J. Zhang, R. Akashi, M. S. Bahramy, R. Arita and Y. Iwasa, *Science*, 2012, **338**, 1193–1196.

This journal is © The Royal Society of Chemistry 2016